# Photochemical aging of aerosols contributes significantly to the production of atmospheric formic acid

Yifan Jiang[1], Men Xia[2,3], Zhe Wang[4], Penggang Zheng[4], Yi Chen[4], and Tao Wang[1]

[1]Department of Civil and Environmental Engineering, The Hong Kong Polytechnic University, Hong Kong SAR 999077, China

[2]Institute for Atmospheric and Earth System Research/Physics, Faculty of Science, University of Helsinki, Helsinki 00014, Finland

[3]Aerosol and Haze Laboratory, Advanced Innovation Center for Soft Matter Science and Engineering, Beijing University of Chemical Technology, 100029, Beijing, China

[4]Division of Environment and Sustainability, Hong Kong University of Science and Technology, Hong Kong SAR 999077, China

*Correspondence to*: Tao Wang (tao.wang@polyu.edu.hk)

## Abstract

Formic acid (HCOOH) is one of the most abundant organic acids in the atmosphere and affects atmospheric acidity and aqueous chemistry. However, the HCOOH sources are not well understood. In a recent field study, we measured atmospheric HCOOH concentrations at a coastal site in South China. The average concentrations of HCOOH were 191 ± 167 ppt in marine air masses and 996 ± 433 ppt in coastal air masses. A strong linear correlation between HCOOH concentrations and the surface area densities of submicron particulate matter was observed in coastal air masses. Post-campaign laboratory experiments confirmed that the photochemical aging of ambient aerosols promoted by heterogeneous reactions with ozone produced a high concentration of HCOOH at a rate of 0.185 ppb h$^{-1}$ under typical ambient conditions at noon time. HCOOH production was strongly affected by nitrate photolysis, as this efficiently produces OH radicals that oxidise organics to form HCOOH. We incorporated this particle-phase source into a photochemical model and the net HCOOH production rate increased by about three times compared with the default Master Chemical Mechanism (MCM). These findings demonstrate that the photochemical aging of aerosols is an important source of HCOOH that should be included in atmospheric chemistry-transport models.

## 1. Introduction

Organic acids are ubiquitous in the troposphere and constitute a significant fraction of the total organics in both the gas and particle phases (Chebbi and Carlier, 1996). They also participate in the aqueous-phase chemistry of clouds, contribute to secondary organic aerosol

(SOA) formation through reactions within the condensed phase (Carlton et al., 2007; Ervens et al., 2004; Lim et al., 2010), and are proposed to enhance the formation of new particles in the atmosphere (Zhang et al., 2004). Formic acid (HCOOH) is among the most abundant organic acids in the atmosphere (Khare et al., 1999) and accounts for over 60% of the free acidity in precipitation in remote areas and more than 30% of that in polluted areas (Andreae et al., 1988; Keene et al., 1983; Keene & Galloway, 1988; Khare et al., 1999; Stavrakou et al., 2012). This contribution is increasingly important due to the decline in the concentrations of anthropogenic nitrogen oxides ($NO_x$) and sulfur dioxide. HCOOH serves as a significant sink of in-cloud hydroxyl radicals ($\cdot$OH) and stabilised Criegee intermediates (SCIs) (Jacob, 1986), and thus influences aqueous-phase chemistry by affecting pH-dependent reaction rates, oxidant concentrations, and solubilities (Vet et al., 2014). HCOOH also plays a role in the formation of cloud condensation nuclei (Yu, 2000), due to its comparatively higher hygroscopicity at low critical supersaturations when incorporated into aerosols (Novakov and Penner, 1993). This, in turn, affects total indirect radiative forcing. Additionally, HCOOH may be involved in halogen chemistry through its heterogeneous reaction with solid sodium chloride in sea-salt aerosols (Xia et al., 2018).

Considering the abovementioned roles of HCOOH in atmospheric chemistry, it is essential to understand its sources and sinks. The main sources of HCOOH include direct emissions from terrestrial vegetation (Andreae et al., 1988), biomass and biofuel burning (Akagi et al., 2011; Goode et al., 2000; Yokelson et al., 2009), fossil-fuel combustion (Kawamura et al., 2000; Zervas et al., 2001a, b) and soil emissions (Sanhueza and Andreae, 1991). The secondary gas-phase formation mechanisms of HCOOH are mainly the oxidation of volatile organic compounds (VOCs), including ozonolysis of terminal alkenes (Neeb et al., 1997), alkyne oxidation (Bohn et al., 1996), OH-initiated isoprene oxidation (Paulot et al., 2009), monoterpene oxidation (Larsen et al., 2001), keto-enol tautomerisation (Andrews et al., 2012; Shaw et al., 2018) and $\cdot$OH oxidation of methyldioxy radicals ($CH_3O_2\cdot$) (Bossolasco et al., 2014). HCOOH is primarily removed from the atmosphere through wet and dry deposition, with a minor sink of being photo-oxidation by $\cdot$OH (Atkinson et al., 2006). However, with these mechanisms included, HCOOH concentrations remain significantly underestimated by previous models (Baboukas et al., 2000; Bannan et al., 2017; Chaliyakunnel et al., 2016; Le Breton et al., 2012; Millet et al., 2015; Yuan et al., 2015), indicating a substantial missing source of HCOOH.

In addition to gas-phase production pathways, HCOOH can also be generated through heterogeneous or condensed-phase processes. Aqueous reactions of formaldehyde (HCHO) (Chameides and Davis, 1983; Jacob, 1986), glyoxal (Carlton et al., 2007) and other species with $\cdot$OH (aq) can produce HCOOH, particularly in moderately acidic environments (Jacob, 1986). A recent chamber experiment has revealed that formaldehyde can be efficiently converted to HCOOH through a multiphase pathway that involves its hydrated form,

methanediol. This pathway has been shown to generate up to four times more formic acid compared to all other known chemical sources combined in a chemistry-climate model, and the modified model largely reproduced observed ambient concentrations of HCOOH (Franco et al., 2021). Moreover, Gao et al. (2022) proposed a new bidirectional deposition-emission process, in which HCOOH deposits rapidly in night-time dew and is re-emitted subsequently from the dew as it evaporates on the following day.

Many laboratory chamber studies have demonstrated that the photochemical aging of organic aerosols can also produce HCOOH (Henry and Donahue, 2012; Malecha and Nizkorodov, 2016; Mang et al., 2008; Pan et al., 2009; Walser et al., 2007; Zhang et al., 2021). The photochemical aging of aerosols occurs through the reactive uptake of oxidants onto particle surfaces, altering their chemical compositions and physical properties (George et al., 2015). In the condensed organic phase, HCOOH can be produced through the photodegradation of SOA (Henry and Donahue, 2012; Malecha and Nizkorodov, 2016). Additionally, the oxidants such as ·OH, nitrogen dioxide ($NO_2$), and nitrite ions/nitrous acid (HONO) produced from the photolysis of particulate nitrate ($NO_3^-$) can also efficiently oxidise organics to produce HCOOH (Zhang et al., 2021). Apart from laboratory experiments, Paulot et al. (2011) observed a marked positive correlation between HCOOH concentrations and submicron organic aerosol masses in field measurements conducted in three distinct areas: coastal, urban, and polar, and suggested that aerosol aging produces HCOOH. The aforementioned results show that there is a need for a quantitative assessment of the contribution of the photochemical aging of aerosols to HCOOH production in the ambient atmosphere.

In this study, we measured HCOOH concentrations at near-ground level at a coastal site in Hong Kong, China, for two months during autumn 2021. We examined the characteristics of HCOOH concentrations and their correlation with related species' concentrations or other parameters. We then conducted a chamber study to measure the rate of HCOOH production during the aging of ambient aerosols and extrapolated the results to the real atmosphere. We incorporated this HCOOH-formation mechanism into a model using a parameterisation involving fine particulate matter concentration, surface area density, light intensity, and ozone ($O_3$) concentration, and then performed simulations to evaluate the HCOOH production rate from the photochemical aging of aerosols. Furthermore, we showed that $NO_3^-$ photolysis acted as a crucial source of ·OH during the aging process. Our results enhanced the understanding of HCOOH sources and model simulations of ambient HCOOH concentrations.

## 2. Methods

2.1. Field observations

Ambient measurements of the atmospheric concentrations of HCOOH and related species/parameters were conducted from 13 August to 31 October 2021 at the Hong Kong

107 Environmental Protection Department's Cape D'Aguilar Super Site (CDSS; 22.21°N,
108 114.25°E), which is situated a few hundred meters away from the nearest coastline of the South
109 China Sea (Fig. S1). During the study period, the air quality of this coastal site was initially
110 predominantly influenced by marine air masses from the South China Sea and subsequently by
111 the coastal air masses transporting regional anthropogenic pollution from East China. The site
112 was also affected by biogenic emissions from local vegetation and ship emissions transported
113 mainly from about 8 kilometres away. There were no other significant anthropogenic sources
114 nearby.

115 The species quantified were HCOOH, HONO, trace gases (nitric oxide, $NO_2$, carbon
116 monoxide (CO), sulfur dioxide ($SO_2$), and $O_3$), volatile organic compounds (VOCs),
117 oxygenated VOCs, aerosol mass concentrations (1-μm particulate matter ($PM_1$), $PM_{2.5}$, and
118 $PM_{10}$ concentrations), aerosol size distributions, aerosol ionic compositions, $NO_2$ photolysis
119 frequency ($jNO_2$), and meteorological parameters (temperature (T), relative humidity (RH),
120 wind direction, and wind speed). A detailed description of the measurement of HCOOH
121 concentration is provided below, and information on other measurements is summarised in
122 Table S1.

123 The concentration of HCOOH was measured at 172.91 atomic mass unit (amu) using an
124 iodide-adduct time-of-flight chemical ionisation mass spectrometer ($I^-$-ToF-CIMS, Aerodyne
125 Research), as we used in our previous study at the same site (Xia et al., 2022). A comprehensive
126 description of the use of the $I^-$-ToF-CIMS can be found in previous studies (Lee et al., 2014;
127 Aljawhary et al., 2013). Briefly, humidified iodomethane-containing $N_2$ air was passed through
128 an inline ioniser (containing polonium-210) to generate iodide ions ($I^-$) and iodide–water ions,
129 which served as the reagent ions, and the HCOOH produced was detected as $IHCOOH^-$. The
130 background concentration of HCOOH was determined every 2 days by injecting zero air and
131 was found to be 60.9 ppt. HCOOH calibration was performed three times on-site and once in
132 the laboratory immediately following the field campaign using diluted gas standards generated
133 by a permeation tube (KIN-TEK) with a permeation rate of 90.87 ng $min^{-1}$. HCOOH sensitivity
134 varies with RH as water competes with HCOOH for $I^-$ (Lee et al., 2014). Thus, the HCOOH
135 sensitivity was measured at various RHs, as shown in Fig. S2. The sensitivity remained stable
136 at a given RH, with a variation of less than 5% throughout the campaign.

137 The ToF-CIMS was housed in an air-conditioned shelter at an indoor air T maintained at
138 25–28 °C. The shelter was located approximately 15 m away from the CDSS station. The
139 sampling tube was a 0.5-m long perfluoroalkoxy-Teflon tube (1/2 in. outer diameter), the inlet
140 of which was situated on the sidewall of the shelter, 1.5 m above the ground. To achieve laminar
141 flow in the sampling tube, a flow rate of 25 Lpm was adopted, with a residence time of 0.1 s.
142 The ToF-CIMS drew ~2 Lpm sample air, and the remaining airflow was discarded. The
143 sampling tube was replaced with a new tube every 2 days to reduce inlet artifacts. We
144 investigated possible inlet artifacts by injecting known concentrations of HCOOH into a used

sampling inlet and found that the artifacts had a negligible effect on the measured HCOOH concentration (difference < 3%). The remaining instruments were housed in the CDSS station, with their sampling inlets located ~1.5 m above the roof.

2.2. Hybrid Single-Particle Lagrangian Integrated Trajectory (HYSPLIT) and Extended Aerosol Inorganic Model IV (E-AIM IV) models

Hourly 24-h backward trajectories were obtained using the HYSPLIT model (https://www.ready.noaa.gov/hypub-bin/trajasrc.pl). The input parameters were Global Data Assimilation System 1° for the meteorology data; 22.21°N and 114.25°E for the location; and 60 m for the endpoint height. Air masses were classified as marine or coastal, based on their source regions. A unique period was identified as a haze period, during which there was a transition from marine air masses to coastal air masses under stagnant conditions (wind speed < 3 m s$^{-1}$). A detailed classification can be found in Fig. S3.

The aerosol water content (AWC) and pH were predicted by the E-AIM IV online in batch mode (http://www.aim.env.uea.ac.uk/aim/model4/model4d.php). The thermodynamic model was constrained by hourly field-measured molar concentrations of $NH_4^+$, sodium ions ($Na^+$), sulfate ions ($SO_4^{2-}$), $NO_3^-$, and chloride ions ($Cl^-$) in $PM_{2.5}$; gas-phase ammonia concentrations; ambient T; and RH. Initial concentrations of protons ($H^+$) and hydroxide ions were estimated based on the ion balance of the major water-soluble ions. The input of $Na^+$ into the model ($Na^+_{(eq)}$) was calculated as a sum of the equivalent concentrations of $Na^+$, potassium ions, magnesium ions, and calcium ions (Eq. (1)). The model also considered water dissociation and allowed all possible solids to form in the system. Parameters p, q, r, and s (options in batch mode) were set to 3, meaning that the input portions of ammonium ($NH_4^+$), $NO_3^-$, $SO_4^{2-}$, and $Cl^-$ always remained in the condensed phase and did not produce corresponding gas-phase species, such as nitric acid ($HNO_3$) and hydrochloric acid. The aqueous-phase $NO_3^-$ concentration was calculated by dividing the moles of aqueous $NO_3^-$ by the AWC. Aerosol pH was calculated as the negative logarithm of the concentration of $H^+$.

$$[Na^+]_{eq} = [Na^+] + [K^+] + 2[Mg^{2+}] + 2[Ca^{2+}] \qquad (1)$$

2.3. Laboratory experiments

We illuminated ambient aerosols collected on filters or aqueous solutions in a dynamic chamber to mimic HCOOH formation in the atmosphere. The overall experimental setup is illustrated in Fig. S4. The dynamic chamber has a dimension of 25-cm length × 15-cm width × 4-cm height with the top side sealed by a transparent Teflon film. Each aerosol filter or solution sample was placed in a quartz Petri dish (inner diameter: 35 mm, inner height: 7 mm) at the chamber's centre. Aerosol filter sampling details can be found in Text S1. A high-pressure xenon (Xe) lamp was used to simulate sunlight and its spectral irradiance is displayed in Fig. 6d. Compared with standard air mass 1.5 solar irradiation (AM 1.5) corresponding to a solar zenith angle of 48.2°, the Xe lamp exhibited a smaller flux at 300–326 nm but a larger flux at 326–420 nm. An air stream from a zero-air generator (Environics, model 7000) served as the

carrier gas that delivered reaction products to the chamber's outflow. The weather conditions that prevailed during the field campaign were mimicked by maintaining the reactor's T at approximately 28 °C and adjusting the RH in the chamber to 70% by passing the carrier gas through a water bubbler. Prior to the introduction of a sample into the chamber, the background HCOOH concentration was monitored for 10 min with the light on and zero air added. After 1 h of irradiation, 100 ppb of $O_3$ was introduced via a dynamic calibrator (Environics® Series 6100) and monitored using an $O_3$ analyser (Thermo Scientific Model 49i). An AM 1.5 filter (which removes light below 360 nm) and a 300–800 nm filter (which allows the passage of 300-800 nm light) were applied to the Xe lamp to investigate the effect of the irradiation wavelength on the formation of HCOOH.

We conducted an experiment to explore the role of nitrate photolysis on the proposed particle-phase mechanism. A sample solution was prepared by mixing formaldehyde (HCHO, Sigma-Aldrich, 37 wt% in water) and sodium nitrate ($NaNO_3$, Honeywell, 99.5% purity). The resulting solution contained 0.15 wt% HCHO and 0.2 M $NaNO_3$, and was adjusted to pH 2.7 by the addition of sulfuric acid ($H_2SO_4$, Sigma-Aldrich, 98% purity), as this was the E-AIM model's prediction of the average aerosol acidity during the entire campaign. We assumed that ·OH produced by $NO_3^-$ photolysis was the rate-limiting species due to its significantly lower abundance relative to organics and HCHO was taken as a representative example of potential precursors of HCOOH. However, it is important to note that the production rate of HCOOH from the oxidation of organics may be overestimated in the solution experiment because ·OH generated by nitrate photolysis can also react with other oxidizable species in the ambient atmosphere.

The average rate of production (ppb·s$^{-1}$) of HCOOH ($P_{HCOOH}$) during the 1-h irradiation was calculated by the following equation (Eq. (2)), derived from (Peng et al., 2022):

$$P_{HCOOH} = \int_0^{60} (C_{HCOOH} - C_{HCOOH-bkg})\, dt \times \frac{Q}{V}/60 \qquad (2)$$

where Q is the carrier gas flow rate (4 L min$^{-1}$); V is the reactor chamber volume (1.875 L); and $C_{HCOOH}$ and $C_{HCOOH-bkg}$ (ppb) are the concentrations of HCOOH in the chamber after and before adding the sample, respectively. The photolytic loss of HCOOH was ignored, as the cross-section of HCOOH was beyond the spectral range of the Xe lamp (Burkholder et al., 2020).

We attempted to extrapolate the laboratory results to account for the field-observed concentrations of HCOOH. As photochemical aging occurs on aerosol surfaces and a strong correlation between the surface area (Sa) and the concentration of HCOOH observed in the field, the extrapolation was conducted based on Sa. The Sa in the chamber was calculated as the Sa of the filter divided by the chamber's volume, assuming that only the first layer of the aerosols was illuminated. Although this might have resulted in an underestimation of the Sa density in the chamber, this assumption was reasonable, because particles in the lower layers

220  would receive less light than those in the uppermost layer due to the light-screening effect of
221  the first layer (Ye et al., 2017). The aging process was also influenced by light intensity, and as
222  we discovered that the major oxidant was generated by the photolysis of particulate $NO_3^-$ (See
223  **Results**, section 2), the light intensity was normalised based on the photolytic frequency of
224  aqueous $NO_3^-$ ($J_{NO_3^-(aq)}$) due to the absence of an absorption coefficient for particulate $NO_3^-$.
225  Although there is a redshift of the particulate $NO_3^-$ absorption wavelength compared with the
226  aqueous-phase $NO_3^-$ absorption wavelength, our results should be reliable because we used
227  $J_{NO_3^-(aq)}$ as a reference for normalisation rather than for calculating an accurate $J_{NO_3^-(aq)}$ (Du
228  and Zhu, 2011; Zhu et al., 2008). The $J_{NO_3^-(aq)}$ under the Xe lamp was $8.85 \times 10^{-6}$ $s^{-1}$ and the
229  daytime average $J_{NO_3^-(aq)}$ in the ambient air at our site was $1.12 \times 10^{-5}$ $s^{-1}$ (Text S2). Both
230  $J_{NO_3^-(aq)}$ values were calculated assuming a quantum yield equal to 1. The normalised HCOOH
231  production rate in the ambient air ($P_{HCOOH-nml}$) was calculated using the following equation (Eq
232  (3)):

$$P_{HCOOH-nml} = P_{HCOOH} \times \frac{Sa_{amb}}{Sa_{cha}} \times 1.266 \qquad (3)$$

234  where $Sa_{amb}$ represents the field-measured Sa density; $Sa_{cha}$ denotes the Sa density calculated
235  for the chamber; and 1.266 is the ratio of the ambient $J_{NO_3^-(aq)}$ to the chamber $J_{NO_3^-(aq)}$. For the
236  aging process involving $O_3$, the photolytic rate constant of $O_3$ generating $O^1D$ ($J_{O_3 \to O^1D}$) in the
237  chamber ($1.31 \times 10^{-5}$ $s^{-1}$) was also normalised to the average daytime $J_{O_3 \to O^1D}$ ($1.84 \times 10^{-5}$ $s^{-1}$)
238  under ambient conditions (Text S2). For the results of the aqueous solution, the
239  concentrations of HCHO and $NO_3^-$ were also normalised.

240  2.4. Chemical box model

241  The Framework for 0-D Atmospheric Modeling (F0AM version 4.2.1) (Wolfe et al., 2016)
242  coupled with Master Chemical Mechanism (MCM v3.3.1, http://mcm.york.ac.uk) (Jenkin et
243  al., 2015) was employed to evaluate the HCOOH production rate from photochemical aging of
244  aerosols compared with other sources at the field site. The physical loss due to dilution process
245  was treated as a first-order loss with a rate coefficient of 1/86,400 $s^{-1}$, consistent with previous
246  studies (Li et al., 2014; Yuan et al., 2015). The dry deposition rate was determined based on the
247  deposition velocity and the boundary layer height (BLH). For HCOOH, a deposition velocity
248  of 1 cm $s^{-1}$ was employed (Müller et al., 2018). A sensitivity analysis of the deposition velocity
249  was also conducted. The diurnal profile of BLH was acquired from a previous study at another
250  coastal site in Hong Kong (Su et al., 2017). Wet deposition was not considered as there was no
251  rainfall except on 3 October and 7 October. We simulated the averaged diurnal cycle for the
252  whole campaign with field-observed relevant species constrained hourly in the model.
253  Simulations were also performed daily for a 2-week period, from 24 September to 7 October.
254  The details of input data are described in Text S3. The model was executed for three replicates
255  to stabilise the intermediate species it generated, and the results from the final run were used

256 for further analysis.

257   The local sources of HCOOH at this site mainly consist of ship and biogenic emissions.
258 The box model used in this study did not account for the contribution of ship emissions since
259 the modelling period was dominated by continental outflows which is unfavourable for the
260 transportation of HCOOH from ship emissions to our site as evidenced by the relatively low
261 concentrations of $NO_x$ in the modelling period. To estimate the biogenic emissions, we used
262 the algorithm of the Model of Emissions of Gases and Aerosols from Nature version 2.1
263 (MEGAN v2.1) (Guenther et al., 2012), assuming instantaneous dilution into the whole box. It
264 is worth noting that this approach may introduce some uncertainties in estimating biogenic
265 emission at a specific location. The specific parameters used can be found in Text S3. For
266 secondary formation mechanisms, we followed Yuan et al. (2015) by enhancing the secondary
267 production of HCOOH by modifying the HCOOH yields obtained by the ozonolysis of alkenes
268 and other unsaturated species, and by adding chemical processes (vinyl alcohol oxidation;
269 photo-tautomerisation of vinyl alcohol; and the reactions of $HCHO + HO_2$ and $CH_3O_2 \cdot + \cdot OH$)
270 to the MCM. However, the model used in this study was unable to account for the downward
271 transport of HCOOH produced in clouds through a newly proposed multiphase pathway
272 (Franco et al., 2021) due to its inability to assess the contribution of vertical mixing and aqueous
273 phase chemistry.

## 3. Results and Discussion

274

### 3.1. Field measurements of HCOOH concentrations

275

276   The field site was exposed to two distinct types of air masses; initially, it was largely
277 exposed to marine air masses, and later to coastal air masses. Marine air masses (T = 29.4 ±
278 2.0 °C, RH = 85.8 ± 7.0 %) were warmer and more humid than coastal air masses (T = 25.7 ±
279 2.3 °C, RH = 77.0 ± 6.0 %), and exhibited low concentrations of $O_3$ (15.0 ± 8.9 ppb) and high
280 concentrations of $NO_x$ (6.2 ± 4.5 ppb). Conversely, coastal air masses were characterised by
281 high concentrations of $O_3$ (53.6 ± 14.2 ppb) and low concentrations of $NO_x$ (1.9 ± 1.6 ppb).
282 The high concentrations of $NO_x$ in the marine air masses are attributable to the emissions from
283 ocean-going container ships that passed the site approximately 8 km to the south. A haze event
284 occurred from 24 September to 2 October, due to a transition from marine to coastal air masses
285 under stagnant conditions. $O_3$ concentrations steadily increased during the first 5 days, peaked
286 on 29 September, and remained high until the end of the haze period (Fig. 1). Therefore, the
287 potential HCOOH formation mechanism was analysed separately for these three distinct
288 periods.

289   Ambient HCOOH concentrations significantly varied during the three periods. The average
290 HCOOH concentration in marine air masses was 191 ± 167 ppt; this was higher than those over
291 the remote ocean, due to local emission sources, but significantly lower than those in urban
292 environments (Table 1). In contrast, the ambient HCOOH concentrations in coastal air masses

were substantially higher, averaging 996 ± 433 ppt, comparable with other measurements at rural or urban background sites. During the haze period, the concentrations of HCOOH displayed a pattern similar to the concentrations of $O_3$, with the daytime peak concentration increasing from 674 to 2790 ppt. A pronounced diurnal variation in the concentration of HCOOH was observed throughout the entire campaign, as illustrated in Fig. 2, consistent with other studies (Millet et al., 2015; Yuan et al., 2015). HCOOH concentrations rapidly increased after sunrise, peaking at approximately 1 pm (local time), and then quickly decreasing in the late afternoon, due to the weaker sunlight and lower BLH than earlier in the day.

HCOOH is widely recognised as a secondary photochemical product. Table 2 presents the Pearson correlation coefficients (r) between the concentration of HCOOH and those of other air pollutants or other meteorological parameters during the three distinct periods. The concentration of $HNO_3$ was strongly correlated with the concentration of HCOOH throughout the entire field campaign, consistent with other studies (Bannan et al., 2017; Millet et al., 2015). This finding suggests that HCOOH is predominantly generated through secondary photochemical mechanisms at this site, as $HNO_3$ is a secondary photochemical product resulting from the reaction between ·OH and $NO_2$. The positive linear relationship between the concentrations of $O_3$ and HCOOH also implies the secondary source of HCOOH.

A previous laboratory study revealed that HCOOH can be produced by the photochemical aging of aerosols (Malecha and Nizkorodov, 2016), which may be an important process in ambient air. In the coastal air masses and haze period, there was a strong correlation between the concentrations of HCOOH and PM, particularly between the concentrations of HCOOH and $PM_1$. This was also observed by Paulot et al. (2011) and suggests that HCOOH may be produced from PM. The Sa of $PM_1$ was also highly correlated with the concentration of HCOOH in both coastal air masses and haze periods, indicating that HCOOH is mainly produced from reactions on aerosol surfaces. However, in the marine air masses, the concentration of HCOOH was not related to aerosols due to the low particle concentrations in such masses. To further explore the potential role of aerosol aging in HCOOH production, we plotted the correlation of HCOOH concentrations with $Sa \times O_3$, $Sa \times NO_3^-$, and $Sa \times O_3 \times NO_3^-$ for the coastal air masses (Fig. 3). We found that the correlation coefficient significantly increased when Sa was combined with the concentration of $O_3$ or $NO_3^-$ or with the concentrations of both species, compared with these three factors being considered separately. This finding suggests that the HCOOH observed in the coastal air masses was not predominantly derived from gas-phase $O_3$ oxidation of VOCs; rather, it was derived from heterogeneous or condensed-phase reactions on aerosol surfaces. The results during the haze period were similar. Therefore, photochemical aerosol aging may play a key role in HCOOH production as the aging process involves the reactive uptake of oxidants onto particle surfaces.

3.2. Laboratory experiments

Figure 4a presents the results of a typical aerosol-filter irradiation experiment. Upon turning

on the light, HCOOH was instantaneously produced, indicating a rapid transfer from the condensed-phase to the gas phase through photochemical reactions. Within 3 minutes, the HCOOH concentration reached 11.1 ppb, but the when the light was turned off, the HCOOH concentration quickly returned to nearly background concentrations. This suggests that HCOOH was produced predominantly via photochemical reactions. The HCOOH concentration exhibited a logarithmic decay after its first peak concentration and this decay also occurred continued after its second peak concentration, which may be attributable to either the evaporative loss of HCOOH or the photochemical loss of oxidants (Ye et al., 2017). When the AM 1.5 filter was added, the HCOOH concentration decreased by approximately 48.1% within 5 min, and after the filter was removed, the HCOOH concentration returned to the logarithmic decay line. This suggests that there was only minor evaporation of HCOOH from the condensed-phase due to the increased temperature of aerosol surfaces under light irradiation. However, the addition of the 300–800 nm filter reduced the HCOOH concentration by only 13.2%, indicating that the photochemical production of HCOOH primarily occurs at wavelengths lower than 360 nm. Given the agreement between the wavelength at which $NO_3^-$ absorbs light (290–350 nm) and the wavelength of HCOOH production ($< 360$ nm), and the high correlation between the ambient HCOOH concentration and the product of Sa density and $NO_3^-$ concentration (as shown in Fig. 3), we infer that ·OH produced from $NO_3^-$ photolysis were the major oxidants in the particle phase and thus drove HCOOH production. The production of HCOOH was also found to be dependent on $O_3$, as the concentration of HCOOH increased by 64.7% after the addition of 100 ppb of $O_3$.

We next extrapolated the production rate of HCOOH observed in the chamber to ambient conditions, using the method described in Section 2.3, to assess the role played by the photochemical aging of aerosols in HCOOH production. Table 3 summarises the HCOOH concentrations and production rates observed in the chamber experiments, and the normalised HCOOH production rates in ambient air under light and light + $O_3$ conditions, respectively. The average $P_{HCOOH-nml}$ without the addition of $O_3$ was determined to be 0.106 ppb h$^{-1}$. The addition of 100 ppb of $O_3$ increased $P_{HCOOH-nml}$ by 0.079 ppb h$^{-1}$, indicating that the heterogenous reaction between $O_3$ and aerosols made a non-negligible contribution to HCOOH production. To quantify the contribution of this particle-phase pathway, we established a relationship between $P_{HCOOH-nml}$ and three parameters: PM$_{2.5}$ concentration (cPM), which represents the reactant concentration; Sa, which represents the available reaction area; and jNO$_2$, which represents the light intensity. After multiplying these three factors, we discovered a strong linear correlation between $P_{HCOOH-nml}$ and cPM × Sa × jNO$_2$ (Fig. 4b). The intercept was set to zero, as there should be no HCOOH production when cPM × Sa × jNO$_2$ is zero. Based on the correlation, we derived an equation (Eq. (4)) for calculating $P_{HCOOH-nml}$ with assumption that $P_{HCOOH-nml (O3)}$ increased linearly with $O_3$ concentration. This equation was then incorporated into a box model to access the importance of this production pathway compared

369    to other sources (See Section 3.3).

370    $P_{HCOOH-nml} = 0.0091x + 0.010_3 \times 0.0064x, \quad x = cPM \times Sa \times jNO_2$       (4)

371    Photolysis of particulate $NO_3^-$ is an important source of ·OH (Zellner et al., 1990; Mack

372    and Bolton, 1999). To investigate the potential production of HCOOH from this source, an

373    irradiation experiment was conducted on a solution (Fig. 4c). The concentration of HCOOH

374    increased linearly with time and did not reach a stable state after 90 min of illumination. This

375    differs from the aerosol experiments and might have been due to the continuous evaporation of

376    water from the solution caused by the heating effect of the light source, which would have

377    concentrated the solution. To determine the appropriate time to calculate $P_{HCOOH}$, we also

378    plotted the time series of HONO concentrations. This showed that the HONO concentration

379    stabilised after 1 h of irradiation, suggesting that $NO_3^-$ photolysis also reached a steady state.

380    As ·OH produced from $NO_3^-$ photolysis were the only oxidants present in the system, the actual

381    HCOOH production rate at the initial HCHO concentration should have followed the same

382    trend as the HONO concentration. Therefore, we chose 1 h after turning on the light as the

383    appropriate time to quantify $P_{HCOOH}$, and found that at this time, $P_{HCOOH}$ in the chamber was

384    21.9 ppt s$^{-1}$.

385    We also attempted to extrapolate the results to ambient air, similar to the aerosol filter

386    experiments. To do so, in addition to normalising Sa and light intensity, we needed to normalise

387    the HCHO and $NO_3^-$ concentrations. The average concentration of gas-phase HCHO (HCHO$_{(g)}$)

388    measured on 28 September was 2.35 µg cm$^{-3}$. By using a ratio of 0.03 between the

389    concentration of HCHO in the particle phase (HCHO$_{(p)}$) and the concentration of HCHO in the

390    gas phase (Toda et al., 2014), the concentration of HCHO$_{(p)}$ was calculated to be 0.07 µg cm$^{-3}$,

391    which is comparable to the concentrations that have been reported in previous studies (Klippel

392    and Warneck, 1980; Toda et al., 2014). Based on the aqueous volume of aerosol calculated by

393    the E-AIM model (0.02 µl m$^{-3}$), the HCHO mass concentration in the aqueous phase was found

394    to be 3.5 g L$^{-1}$. The $NO_3^-$ concentration on the aerosol surface was determined to be 0.98 mol

395    L$^{-1}$. Therefore, the $P_{HCOOH}$ in ambient air attributable to the aqueous oxidation of HCHO was

396    estimated to be 0.41 ppb h$^{-1}$, which is 285% higher than the $P_{HCOOH}$ attributable to the

397    photochemical aging of ambient particles. This greater-than-100% contribution could be

398    attributable to the simplicity of the solution system. In ambient air, other oxidisable species,

399    such as halides (Peng et al., 2022; M. Xia et al., 2022) could also react with the ·OH produced

400    from $NO_3^-$ photolysis, which competes with HCHO. In summary, $NO_3^-$ photolysis appears to

401    be a critical source of oxidants during the photochemical aging process of aerosols.

402    3.3. Box model simulation

403    We next use a box model (see Methods 2.4) to evaluate the production and loss of HCOOH

404    in four scenarios (Table 4) which include the default MCM mechanism (S1), modified with

405    gas-phase reactions following Yuan et al. (2015) (S2), further addition of the photochemical

406    aging source (S3), and further adding of a biogenic source (S4). Figure 5 presents a

407  comprehensive analysis of HCOOH budget of campaign-averaged diurnal profile. In the base

408  case (Default MCM), the highest net production rate of HCOOH ($P_{HCOOH-net}$) is 0.018 ppb h$^{-1}$,

409  significantly lower than the observed average rate of increase in HCOOH concentrations of

410  0.095 ppb h$^{-1}$ from 6 am to 1 pm. Despite an increase of $P_{HCOOH-net}$ to 0.031 ppb h$^{-1}$ in modified

411  case, the modelled value still lower than the observed rate of change. In both cases, the reaction

412  of $CH_2OO$ Criegee intermediate biradicals with $H_2O$ was identified as the major source of

413  HCOOH, accounting for about 68% of the currently known sources. $CH_2OO$ is formed from

414  seven excited biradicals that originate from the $O_3$ oxidation of various alkenes and unsaturated

415  compounds (Saunders et al., 2003). Among these, $CH_2OOE$ is the largest contributor to the

416  production of $CH_2OO$ (Fig. S5) and is generated by the ozonolysis of isoprene.

417     Incorporating the photochemical production of HCOOH from particles into the F0AM

418  model (S3) resulted in substantial improvements in predictions. The peak $P_{HCOOH-net}$ increased

419  to 0.073 ppb h$^{-1}$, which is more than double that of the modified case. Among the secondary

420  production mechanisms considered, the production of HCOOH from particles was found to be

421  the largest source, accounting for 52.1% of the secondary production (Fig. 5c). The biogenic

422  emissions (S4) also played an important role, contributing to 34.4% of the total production (Fig.

423  5d). After considering all sources, including primary emissions and secondary productions, the

424  modelled $P_{HCOOH-net}$ (0.094 ppb h$^{-1}$) was much closer to the observed increase rate of HCOOH

425  (0.095 ppb h$^{-1}$).

426     Figure 6 presents the observed and modelled concentrations of HCOOH using different

427  mechanisms for the averaged diurnal profile throughout the whole campaign. It is evident that

428  the predicted HCOOH concentration increased substantially after incorporating the

429  productions from the photochemical aging of aerosols. However, the modelled HCOOH

430  concentration is still lower than the observed value in Scenario 4, where all sources are included.

431  The discrepancy may be explained by the inadequate treatment of physical processes in the box

432  model, such as deposition, convection, and advection. The primary loss of HCOOH is via

433  deposition, owing to its high solubility in water. To account for uncertainty in the deposition

434  velocity ($V_d$) of HCOOH, we conducted a sensitivity test of HCOOH production to various $V_d$

435  values in Scenario 4 (Fig. S6). The results revealed that a smaller deposition velocity results in

436  higher modelled HCOOH concentrations. The daytime peak concentration increased by about

437  20% when $V_d$ decreased from 1.00 to 0.50 cm s$^{-1}$. The field-observed $V_d$ of HCOOH ranges

438  from 0.43 cm s$^{-1}$ to 1.10 cm s$^{-1}$ (Müller et al., 2018), and thus given the high humidity at the

439  study site, the observed $V_d$ of HCOOH of 0.5 cm s$^{-1}$ should have been close to the lower limit.

440  Although the modelled concentration with $V_d = 0.50$ cm s$^{-1}$ were similar to observed values,

441  the model failed to accurately predict the timing of the initial increase, peak, and sharp decrease

442  in HCOOH concentrations, indicating that other physical process, such as vertical mixing, also

443  influence the HCOOH concentration. Therefore, to account for the complex physical processes,

444  we employed a bimodal physical loss rate due to vertical dilution that varied with time of day

445    (1/21,600 $s^{-1}$ in daytime and a much smaller value of 1/518,400 $s^{-1}$ at night), as suggested by

446    Yuan et al. (2015). It is clear that the model performed better in predicting the diurnal pattern

447    using the bimodal physical loss rate compared to a constant value (Fig. 6).

448        After applying a bimodal physical loss rate, the model also predicts better in the continuous

449    simulation of two weeks (Fig. S7), except for 30 September and 1 October. The observed

450    HCOOH concentrations on these two days were significantly lower than the modelled values

451    due to a lower nitrate proportion (13.5%) on 30 September compared to other days during the

452    model period (22.2%). Therefore, the simplified parameterization using $PM_{2.5}$ may

453    overestimate the production of HCOOH from photochemical aging of aerosols in areas with

454    high PM concentrations but a low nitrate proportion. An improved parameterization using the

455    concentrations of nitrate and organics should be developed in future studies.

456        To evaluate the role of aerosol photochemical aging on HCOOH production in a broader

457    context, we also examined the HCOOH data over the remote marine boundary layer obtained

458    from the Atmospheric Tomography Mission (ATom) aircraft campaign which was conducted

459    around the globe during April-May 2018 (Wofsy et al., 2021) (Text S5). Our results show that

460    the photochemical aging of aerosols was insignificant in remote ocean areas due to the low PM

461    and nitrate concentrations found there. However, when these regions are affected by aged fire

462    plumes containing higher levels of organics and nitrate, photochemical aging of aerosols

463    accounts for the substantial sources of HCOOH. These results suggest the photochemical aging

464    appears to be important in relatively polluted atmospheres.

## 465   4. Conclusion and implications

466        This study demonstrates high rates of HCOOH production from the photochemical aging

467    of real ambient particles and the potential importance of this pathway in the formation of

468    HCOOH under ambient conditions at a coastal site in Hong Kong. Incorporating aerosol

469    photochemical aging significantly improved the performance of a widely used chemical model,

470    which underscores the significance of condensed-phase photochemistry and the necessity of

471    incorporating its mechanisms into atmospheric models. The substantial production of HCOOH

472    from condensed-phase photochemical reactions altered both the composition and the volatility

473    of SOA. Moreover, other low-molecular-weight organic acids, such as acetic acid, may be

474    produced via this mechanism, as observed in our irradiation experiments. Improving the

475    constraints on this photochemical aging of aerosols will not only aid the understanding of the

476    budget of these organic acids but also affect their SOA chemistry.

477        Our solution irradiation experiments demonstrated the crucial role of $NO_3^-$ photolysis in

478    HCOOH production via the production of ·OH. This suggests that $NO_3^-$ photolysis not only

479    influences the aerosol-based production of inorganic species (such as HONO (Ye et al., 2017)

480    and halogens (Peng et al., 2022; M. Xia et al., 2022)), but also the aerosol-based production of

481    water-soluble organics. Therefore, future investigations into the involvement of $NO_3^-$

photodissociation in aerosol aging processes are necessary to enhance our understanding of the underlying mechanisms in the photochemical aging of aerosols.

## Data availability

The data that support the findings of this study are openly available in Zenodo at https://10.5281/zenodo.8415792. Other raw data are also available from the corresponding author, upon reasonable request.

## Authors' contributions

T. W. arranged the field campaign and designed the laboratory irradiation experiment. Y. J. and M. X. conducted the field campaign and photochemical filter experiments. M. X. revised the model code. Y. J. conducted the photochemical solution experiments, analysed the data, ran the model, and wrote the draft manuscript. T. W. and M. X. revised the manuscript.

## Competing interests

One author (Tao Wang) is a member of the editorial board of Atmospheric Chemistry and Physics. The authors have no other competing interests to declare.

## Acknowledgements

We thank the Hong Kong Environmental Protection Department for allowing us to use the field study site and for providing data on VOCs, OVOCs, trace gases, PM mass concentrations, and ion compositions; the Hong Kong Observatory for providing the meteorological data; the Hong Kong Polytechnic University Research Facility in Chemical and Environmental Analysis for providing the ToF-CIMS; and Dr Zhao Jue for providing $PM_{2.5}$ filters, whose work is supported by projects (PolyU Project of Strategic Importance No. ZE2K and RGC-GRF No. 15203920). We are grateful to Steven Poon for his help with logistics.

## Funding

This work was supported by the Research Grants Council of the Hong Kong (Project No. T24/504/17).

## References

Akagi, S. K., Yokelson, R. J., Wiedinmyer, C., Alvarado, M. J., Reid, J. S., Karl, T., Crounse, J. D., and Wennberg, P. O.: Atmospheric Chemistry and Physics Emission factors for open and domestic biomass burning for use in atmospheric models, Atmos. Chem. Phys, 11, 4039–4072,

https://doi.org/10.5194/acp-11-4039-2011, 2011.

Aljawhary, D., Lee, A. K. Y., and Abbatt, J. P. D.: High-resolution chemical ionization mass spectrometry (ToF-CIMS): Application to study SOA composition and processing, Atmos Meas Tech, 6, 3211–3224, https://doi.org/10.5194/amt-6-3211-2013, 2013.

Andreae, M. O., Talbot, R. W., Andreae, T. W., and Harriss, R. C.: Formic and acetic acid over the central Amazon region, Brazil: 1. Dry season, J. Geophys. Res. Atmos., 93, 1616–1624, https://doi.org/10.1029/JD093ID02P01616, 1988.

Andrews, D. U., Heazlewood, B. R., Maccarone, A. T., Conroy, T., Payne, R. J., Jordan, M. J. T., and Kable, S. H.: Photo-tautomerization of acetaldehyde to vinyl alcohol: A potential route to tropospheric acids, Science, 337, 1203–1206, https://doi.org/10.1126/SCIENCE.1220712, 2012.

Atkinson, R., Baulch, D. L., Cox, R. A., Crowley, J. N., Hampson, R. F., Hynes, R. G., Jenkin, M. E., Rossi, M. J., and Troe, J.: Evaluated kinetic and photochemical data for atmospheric chemistry: Volume II - Gas phase reactions of organic species, Atmos. Chem. Phys, 6, 3625–4055, https://doi.org/10.5194/ACP-6-3625-2006, 2006.

Baboukas, E. D., Kanakidou, M., and Mihalopoulos, N.: Carboxylic acids in gas and particulate phase above the Atlantic Ocean, J. Geophys. Res. Atmos, 105, 14459–14471, https://doi.org/10.1029/1999JD900977, 2000.

Bannan, T. J., Murray Booth, A., le Breton, M., Bacak, A., Muller, J. B. A., Leather, K. E., Khan, M. A. H., Lee, J. D., Dunmore, R. E., Hopkins, J. R., Fleming, Z. L., Sheps, L., Taatjes, C. A., Shallcross, D. E., and Percival, C. J.: Seasonality of Formic Acid (HCOOH) in London during the ClearfLo Campaign, J. Geophys. Res. Atmos, 122, 12,488-12,498, https://doi.org/10.1002/2017JD027064, 2017.

Bohn, B., Siese, M., and Zetzschn, C.: Kinetics of the OH + C2H2 reaction in the presence of O2, Journal of the Chemical Society, Faraday Transactions, 92, 1459–1466, https://doi.org/10.1039/FT9969201459, 1996.

Bossolasco, A., Faragó, E. P., Schoemaecker, C., and Fittschen, C.: Rate constant of the reaction between CH3O2 and OH radicals, Chem Phys Lett, 593, 7–13, https://doi.org/10.1016/J.CPLETT.2013.12.052, 2014.

Burkholder, J. B., Sander, S. P., Abbatt, J. P. D., Barker, J. R., Cappa, C., Crounse, J. D., Dibble, T. S., Huie, R. E., Kolb, C. E., Kurylo, M. J., Orkin, V. L., Percival, C. J., Wilmouth, D. M., and Wine, P. H.: Chemical kinetics and photochemical data for use in atmospheric studies; evaluation number 19, 2020.

Carlton, A. G., Turpin, B. J., Altieri, K. E., Seitzinger, S., Reff, A., Lim, H. J., and Ervens, B.: Atmospheric oxalic acid and SOA production from glyoxal: Results of aqueous photooxidation experiments, Atmos Environ, 41, 7588–7602, https://doi.org/10.1016/J.ATMOSENV.2007.05.035, 2007.

Chaliyakunnel, S., Millet, D. B., Wells, K. C., Cady-Pereira, K. E., and Shephard, M. W.: A

Large Underestimate of Formic Acid from Tropical Fires: Constraints from Space-Borne Measurements, Environ Sci Technol, 50, 5631–5640, https://doi.org/10.1021/acs.est.5b06385, 2016.

Chameides, W. L. and Davis, D. D.: Aqueous-phase source of formic acid in clouds, Nature, 304, 427–429, https://doi.org/10.1038/304427a0, 1983.

Chebbi, A. and Carlier, P.: Carboxylic acids in the troposphere, occurrence, sources, and sinks: A review, Atmos Environ, 30, 4233–4249, https://doi.org/10.1016/1352-2310(96)00102-1, 1996.

Chen, X., Millet, D. B., Neuman, J. A., Veres, P. R., Ray, E. A., Commane, R., Daube, B. C., McKain, K., Schwarz, J. P., Katich, J. M., Froyd, K. D., Schill, G. P., Kim, M. J., Crounse, J. D., Allen, H. M., Apel, E. C., Hornbrook, R. S., Blake, D. R., Nault, B. A., Campuzano-Jost, P., Jimenez, J. L., and Dibb, J. E.: HCOOH in the Remote Atmosphere: Constraints from Atmospheric Tomography (ATom) Airborne Observations, ACS Earth Space Chem, 5, 1436–1454, https://doi.org/10.1021/acsearthspacechem.1c00049, 2021.

Du, J. and Zhu, L.: Quantification of the absorption cross sections of surface-adsorbed nitric acid in the 335-365 nm region by Brewster angle cavity ring-down spectroscopy, Chem Phys Lett, 511, 213–218, https://doi.org/10.1016/j.cplett.2011.06.062, 2011.

Ervens, B., Feingold, G., Frost, G. J., and Kreidenweis, S. M.: A modeling study of aqueous production of dicarboxylic acids: 1. Chemical pathways and speciated organic mass production, J. Geophys. Res. Atmos, 109, https://doi.org/10.1029/2003JD004387, 2004.

Franco, B., Blumenstock, T., Cho, C., Clarisse, L., Clerbaux, C., Coheur, P. F., De Mazière, M., De Smedt, I., Dorn, H. P., Emmerichs, T., Fuchs, H., Gkatzelis, G., Griffith, D. W. T., Gromov, S., Hannigan, J. W., Hase, F., Hohaus, T., Jones, N., Kerkweg, A., Kiendler-Scharr, A., Lutsch, E., Mahieu, E., Novelli, A., Ortega, I., Paton-Walsh, C., Pommier, M., Pozzer, A., Reimer, D., Rosanka, S., Sander, R., Schneider, M., Strong, K., Tillmann, R., Van Roozendael, M., Vereecken, L., Vigouroux, C., Wahner, A., and Taraborrelli, D.: Ubiquitous atmospheric production of organic acids mediated by cloud droplets, Nature, 593, 233–237, https://doi.org/10.1038/s41586-021-03462-x, 2021.

Fulgham, S. R., Brophy, P., Link, M., Ortega, J., Pollack, I., and Farmer, D. K.: Seasonal Flux Measurements over a Colorado Pine Forest Demonstrate a Persistent Source of Organic Acids, ACS Earth Space Chem, 3, 2017–2032, https://doi.org/10.1021/acsearthspacechem.9b00182, 2019.

Gao, Z., Vasilakos, P., Nah, T., Takeuchi, M., Chen, H., Tanner, D. J., Ng, N. L., Kaiser, J., Huey, L. G., Weber, R. J., and Russell, A. G.: Emissions, chemistry or bidirectional surface transfer? Gas phase formic acid dynamics in the atmosphere, Atmos Environ, 274, https://doi.org/10.1016/J.ATMOSENV.2022.118995, 2022.

George, C., Ammann, M., D'Anna, B., Donaldson, D. J., and Nizkorodov, S. A.: Heterogeneous Photochemistry in the Atmosphere, Chem Rev, 115, 4218–4258,

https://doi.org/10.1021/cr500648z, 2015.

Goode, J. G., Yokelson, R. J., Ward, D. E., Susott, R. A., Babbitt, R. E., Davies, M. A., and Hao, W. M.: Measurements of excess $O_3$, $CO_2$, CO, $CH_4$, $C_2H_4$, $C_2H_2$, HCN, NO, $NH_3$, HCOOH, $CH_3COOH$, HCHO, and $CH_3OH$ in 1997 Alaskan biomass burning plumes by airborne Fourier transform infrared spectroscopy (AFTIR), J. Geophys. Res. Atmos, 105, 22147–22166, https://doi.org/10.1029/2000JD900287, 2000.

Guenther, A. B., Jiang, X., Heald, C. L., Sakulyanontvittaya, T., Duhl, T., Emmons, L. K., and Wang, X.: The Model of Emissions of Gases and Aerosols from Nature version 2.1 (MEGAN2.1): an extended and updated framework for modeling biogenic emissions, Geosci. Model Dev, 5, 1471–1492, https://doi.org/10.5194/gmd-5-1471-2012, 2012.

Henry, K. M. and Donahue, N. M.: Photochemical Aging of α-Pinene Secondary Organic Aerosol: Effects of OH Radical Sources and Photolysis, J Phys Chem A, 116, 5932–5940, https://doi.org/10.1021/jp210288s, 2012.

Jacob, D. J.: Chemistry of OH in remote clouds and its role in the production of formic acid and peroxymonosulfate, J Geophys Res, 91, 9807, https://doi.org/10.1029/JD091ID09P09807, 1986.

Jenkin, M. E., Young, J. C., and Rickard, A. R.: The MCM v3.3.1 degradation scheme for isoprene, Atmos Chem Phys, 15, 11433–11459, https://doi.org/10.5194/ACP-15-11433-2015, 2015.

Kawamura, K., Steinberg, S., and Kaplan, I. R.: Homologous series of C1-C10 monocarboxylic acids and C1-C6 carbonyls in Los Angeles air and motor vehicle exhausts, Atmos Environ, 34, 4175–4191, https://doi.org/10.1016/S1352-2310(00)00212-0, 2000.

Keene, W. C. and Galloway, J. N.: The biogeochemical cycling of formic and acetic acids through the troposphere: an overview of current understanding, Chem Phys Meteorol, 40, 322–334, https://doi.org/10.3402/tellusb.v40i5.15994, 1988.

Keene, W. C., Galloway, J. N., and Holden, J. D.: Measurement of weak organic acidity in precipitation from remote areas of the world, J Geophys Res, 88, 5122–5130, https://doi.org/10.1029/JC088IC09P05122, 1983.

Khare, P., Kumar, N., Kumari, K. M., and Srivastava, S. S.: Atmospheric formic and acetic acids: An overview, Reviews of Geophysics, 37, 227–248, https://doi.org/10.1029/1998RG900005, 1999.

Klippel, W. and Warneck, P.: The formaldehyde content of the atmospheric aerosol, Atmos Environ, 14, 809–818, https://doi.org/10.1016/0004-6981(80)90137-7, 1980.

Larsen, B. R., di Bella, D., Glasius, M., Winterhalter, R., Jensen, N. R., and Hjorth, J.: Gas-Phase OH Oxidation of Monoterpenes: Gaseous and Particulate Products, J Atmos Chem, 38, 231–276, https://doi.org/10.1023/A:1006487530903, 2001.

Le Breton, M., McGillen, M. R., Muller, J. B. A., Bacak, A., Shallcross, D. E., Xiao, P., Huey, L. G., Tanner, D., Coe, H., and Percival, C. J.: Airborne observations of formic acid using a

625 chemical ionization mass spectrometer, Atmos Meas Tech, 5, 3029–3039,
626 https://doi.org/10.5194/amt-5-3029-2012, 2012.

627 Lee, B. H., Lopez-Hilfiker, F. D., Mohr, C., Kurtén, T., Worsnop, D. R., and Thornton, J. A.:
628 An iodide-adduct high-resolution time-of-flight chemical-ionization mass spectrometer:
629 Application to atmospheric inorganic and organic compounds, Environ Sci Technol, 48, 6309–
630 6317, https://doi.org/10.1021/es500362a, 2014.

631 Li, X., Rohrer, F., Brauers, T., Hofzumahaus, A., Lu, K., Shao, M., Zhang, Y. H., and Wahner,
632 A.: Modeling of HCHO and CHOCHO at a semi-rural site in southern China during the
633 PRIDE-PRD2006 campaign, Atmos Chem Phys, 14, 12291–12305,
634 https://doi.org/10.5194/ACP-14-12291-2014, 2014.

635 Lim, Y. B., Tan, Y., Perri, M. J., Seitzinger, S. P., and Turpin, B. J.: Aqueous chemistry and its
636 role in secondary organic aerosol (SOA) formation, Atmos Chem Phys, 10, 10521–10539,
637 https://doi.org/10.5194/ACP-10-10521-2010, 2010.

638 Mack, J. and Bolton, J. R.: Photochemistry of nitrite and nitrate in aqueous solution: a review,
639 J Photochem Photobiol A Chem, 128, 1–13, https://doi.org/10.1016/S1010-6030(99)00155-0,
640 1999.

641 Malecha, K. T. and Nizkorodov, S. A.: Photodegradation of Secondary Organic Aerosol
642 Particles as a Source of Small, Oxygenated Volatile Organic Compounds, Environ. Sci. Technol,
643 50, 9990–9997, https://doi.org/10.1021/acs.est.6b02313, 2016.

644 Mang, S. A., Henricksen, D. K., Bateman, A. E., Andersen, M. P. S., Blake, D. R., and
645 Nizkorodov, S. A.: Contribution of carbonyl photochemistry to aging of atmospheric secondary
646 organic aerosol, J. Phys. Chem. A, 112, 8337–8344, https://doi.org/10.1021/jp804376c, 2008.

647 Millet, D. B., Baasandorj, M., Farmer, D. K., Thornton, J. A., Baumann, K., Brophy, P.,
648 Chaliyakunnel, S., De Gouw, J. A., Graus, M., Hu, L., Koss, A., Lee, B. H., Lopez-Hilfiker, F.
649 D., Neuman, J. A., Paulot, F., Peischl, J., Pollack, I. B., Ryerson, T. B., Warneke, C., Williams,
650 B. J., and Xu, J.: A large and ubiquitous source of atmospheric formic acid, Atmos Chem Phys,
651 15, 6283–6304, https://doi.org/10.5194/acp-15-6283-2015, 2015.

652 Miyazaki, Y., Sawano, M., and Kawamura, K.: Low-molecular-weight hydroxyacids in marine
653 atmospheric aerosol: Evidence of a marine microbial origin, Biogeosciences, 11, 4407–4414,
654 https://doi.org/10.5194/BG-11-4407-2014, 2014.

655 Müller, J.-F., Stavrakou, T., Bauwens, M., Compernolle, S., and Peeters, J.: Chemistry and
656 deposition in the Model of Atmospheric composition at Global and Regional scales using
657 Inversion Techniques for Trace gas Emissions (MAGRITTE v1.0). Part B. Dry deposition,
658 Geosci. Model Dev. Discuss. [preprint], https://doi.org/10.5194/gmd-2018-317, 2018.

659 Nah, T., Guo, H., Sullivan, A. P., Chen, Y., Tanner, D. J., Nenes, A., Russell, A., Lee Ng, N.,
660 Gregory Huey, L., and Weber, R. J.: Characterization of aerosol composition, aerosol acidity,
661 and organic acid partitioning at an agriculturally intensive rural southeastern US site, Atmos
662 Chem Phys, 18, 11471–11491, https://doi.org/10.5194/ACP-18-11471-2018, 2018.

663 Neeb, P., Sauer, F., Horie, O., and Moortgat, G. K.: Formation of hydroxymethyl hydroperoxide
664 and formic acid in alkene ozonolysis in the presence of water vapour, Atmos Environ, 31,
665 1417–1423, https://doi.org/10.1016/S1352-2310(96)00322-6, 1997.

666 Novakov, T. and Penner, J. E.: Large contribution of organic aerosols to cloud-condensation-
667 nuclei concentrations, Nature, 365, 823–826, https://doi.org/10.1038/365823a0, 1993.

668 Pan, X., Underwood, J. S., Xing, J. H., Mang, S. A., and Nizkorodov, S. A.: Photodegradation
669 of secondary organic aerosol generated from limonene oxidation by ozone studied with
670 chemical ionization mass spectrometry, Atmos Chem Phys, 9, 3851–3865,
671 https://doi.org/10.5194/ACP-9-3851-2009, 2009.

672 Paulot, F., Crounse, J. D., Kjaergaard, H. G., Kroll, J. H., Seinfeld, J. H., and Wennberg, P. O.:
673 Isoprene photooxidation: New insights into the production of acids and organic nitrates, Atmos
674 Chem Phys, 9, 1479–1501, https://doi.org/10.5194/acp-9-1479-2009, 2009.

675 Paulot, F., Wunch, D., Crounse, J. D., Toon, G. C., Millet, D. B., Decarlo, P. F., Vigouroux, C.,
676 Deutscher, N. M., Abad, G. G., Notholt, J., Warneke, T., Hannigan, J. W., Warneke, C., De
677 Gouw, J. A., Dunlea, E. J., De Mazière, M., Griffith, D. W. T., Bernath, P., Jimenez, J. L., and
678 Wennberg, P. O.: Importance of secondary sources in the atmospheric budgets of formic and
679 acetic acids, Atmos Chem Phys, 11, 1989–2013, https://doi.org/10.5194/acp-11-1989-2011,
680 2011.

681 Peng, X., Wang, T., Wang, W., Ravishankara, A. R., George, C., Xia, M., Cai, M., Li, Q.,
682 Salvador, C. M., Lau, C., Lyu, X., Poon, C. N., Mellouki, A., Mu, Y., Hallquist, M., Saiz-Lopez,
683 A., Guo, H., Herrmann, H., Yu, C., Dai, J., Wang, Y., Wang, X., Yu, A., Leung, K., Lee, S., and
684 Chen, J.: Photodissociation of particulate nitrate as a source of daytime tropospheric Cl2, Nat
685 Commun, 13, https://doi.org/10.1038/s41467-022-28383-9, 2022.

686 Sanhueza, E. and Andreae, M. O.: Emission of formic and acetic acids from tropical Savanna
687 soils, Geophys Res Lett, 18, 1707–1710, https://doi.org/10.1029/91GL01565, 1991.

688 Saunders, S. M., Jenkin, M. E., Derwent, R. G., and Pilling, M. J.: Protocol for the development
689 of the Master Chemical Mechanism, MCM v3 (Part A): Tropospheric degradation of non-
690 aromatic volatile organic compounds, Atmos Chem Phys, 3, 161–180,
691 https://doi.org/10.5194/ACP-3-161-2003, 2003.

692 Shaw, M. F., Sztáray, B., Whalley, L. K., Heard, D. E., Millet, D. B., Jordan, M. J. T., Osborn,
693 D. L., and Kable, S. H.: Photo-tautomerization of acetaldehyde as a photochemical source of
694 formic acid in the troposphere, Nat Commun, 9, 1–7, https://doi.org/10.1038/s41467-018-
695 04824-2, 2018.

696 Stavrakou, T., Müller, J. F., Peeters, J., Razavi, A., Clarisse, L., Clerbaux, C., Coheur, P. F.,
697 Hurtmans, D., De Mazière, M., Vigouroux, C., Deutscher, N. M., Griffith, D. W. T., Jones, N.,
698 and Paton-Walsh, C.: Satellite evidence for a large source of formic acid from boreal and
699 tropical forests, Nat Geosci, 5, 26–30, https://doi.org/10.1038/ngeo1354, 2012.

700 Su, T., Li, J., Li, C., Xiang, P., Lau, A. K. H., Guo, J., Yang, D., and Miao, Y.: An

intercomparison of long-term planetary boundary layer heights retrieved from CALIPSO, ground-based lidar, and radiosonde measurements over Hong Kong, J. Geophys. Res. Atmos, 122, 3929–3943, https://doi.org/10.1002/2016JD025937, 2017.

Toda, K., Yunoki, S., Yanaga, A., Takeuchi, M., Ohira, S.-I., and Dasgupta, P. K.: Formaldehyde Content of Atmospheric Aerosol, Environ Sci Technol, 48, 6636–6643, https://doi.org/10.1021/es500590e, 2014.

Vet, R., Artz, R. S., Carou, S., Shaw, M., Ro, C. U., Aas, W., Baker, A., Bowersox, V. C., Dentener, F., Galy-Lacaux, C., Hou, A., Pienaar, J. J., Gillett, R., Forti, M. C., Gromov, S., Hara, H., Khodzher, T., Mahowald, N. M., Nickovic, S., Rao, P. S. P., and Reid, N. W.: A global assessment of precipitation chemistry and deposition of sulfur, nitrogen, sea salt, base cations, organic acids, acidity and pH, and phosphorus, Atmos Environ, 93, 3–100, https://doi.org/10.1016/J.ATMOSENV.2013.10.060, 2014.

Walser, M. L., Park, J., Gomez, A. L., Russell, A. R., and Nizkorodov, S. A.: Photochemical Aging of Secondary Organic Aerosol Particles Generated from the Oxidation of d-Limonene, https://doi.org/10.1021/jp662293l, 2007.

Wofsy, S.C., S. Afshar, H.M. Allen, E.C. Apel, E.C. Asher, B. Barletta, J. Bent, H. Bian, B.C. Biggs, D.R. Blake, N. Blake, I. Bourgeois, C.A. Brock, W.H. Brune, J.W. Budney, T.P. Bui, A. Butler, P. Campuzano-Jost, C.S. Chang, M. Chin, R. Commane, G. Correa, J.D. Crounse, P. D. Cullis, B.C. Daube, D.A. Day, J.M. Dean-Day, J.E. Dibb, J.P. DiGangi, G.S. Diskin, M. Dollner, J.W. Elkins, F. Erdesz, A.M. Fiore, C.M. Flynn, K.D. Froyd, D.W. Gesler, S.R. Hall, T.F. Hanisco, R.A. Hannun, A.J. Hills, E.J. Hintsa, A. Hoffman, R.S. Hornbrook, L.G. Huey, S. Hughes, J.L. Jimenez, B.J. Johnson, J.M. Katich, R.F. Keeling, M.J. Kim, A. Kupc, L.R. Lait, K. McKain, R.J. Mclaughlin, S. Meinardi, D.O. Miller, S.A. Montzka, F.L. Moore, E.J. Morgan, D.M. Murphy, L.T. Murray, B.A. Nault, J.A. Neuman, P.A. Newman, J.M. Nicely, X. Pan, W. Paplawsky, J. Peischl, M.J. Prather, D.J. Price, E.A. Ray, J.M. Reeves, M. Richardson, A.W. Rollins, K.H. Rosenlof, T.B. Ryerson, E. Scheuer, G.P. Schill, J.C. Schroder, J.P. Schwarz, J.M. St.Clair, S.D. Steenrod, B.B. Stephens, S.A. Strode, C. Sweeney, D. Tanner, A.P. Teng, A.B. Thames, C.R. Thompson, K. Ullmann, P.R. Veres, N.L. Wagner, A. Watt, R. Weber, B.B. Weinzierl, P.O. Wennberg, C.J. Williamson, J.C. Wilson, G.M. Wolfe, C.T. Woods, L.H. Zeng, and N. Vieznor.: ATom: Merged Atmospheric Chemistry, Trace Gases, and Aerosols, Version 2 (Version 2.0), ORNL Distributed Active Archive Center, https://doi.org/10.3334/ornldaac/1925, 2021.

Wolfe, G. M., Marvin, M. R., Roberts, S. J., Travis, K. R., and Liao, J.: The framework for 0-D atmospheric modeling (F0AM) v3.1, Geosci Model Dev, 9, 3309–3319, https://doi.org/10.5194/GMD-9-3309-2016, 2016.

Xia, K., Tong, S., Zhang, Y., Tan, F., Chen, Y., Zhang, W., Guo, Y., Jing, B., Ge, M., Zhao, Y., Alamry, K. A., Marwani, H. M., and Wang, S.: Heterogeneous Reaction of HCOOH on NaCl Particles at Different Relative Humidities, J. Phys. Chem. A, 122, 7218–7226,

https://doi.org/10.1021/acs.jpca.8b02790, 2018.

Xia, M., Wang, T., Wang, Z., Chen, Y., Peng, X., Huo, Y., Wang, W., Yuan, Q., Jiang, Y., Guo, H., Lau, C., Leung, K., Yu, A., and Lee, S.: Pollution-Derived Br 2 Boosts Oxidation Power of the Coastal Atmosphere, Environ. Sci. Technol, 56, 12055–12065, https://doi.org/10.1021/acs.est.2c02434, 2022.

Xu, J., Chen, J., Shi, Y., Zhao, N., Qin, X., Yu, G., Liu, J., Lin, Y., Fu, Q., Weber, R. J., Lee, S. H., Deng, C., and Huang, K.: First Continuous Measurement of Gaseous and Particulate Formic Acid in a Suburban Area of East China: Seasonality and Gas-Particle Partitioning, ACS Earth Space Chem, 4, 157–167, https://doi.org/10.1021/acsearthspacechem.9b00210, 2020.

Ye, C., Zhang, N., Gao, H., and Zhou, X.: Photolysis of Particulate Nitrate as a Source of HONO and NOx, Environ Sci Technol, 51, 6849–6856, https://doi.org/10.1021/acs.est.7b00387, 2017.

Yokelson, R. J., Crounse, J. D., DeCarlo, P. F., Karl, T., Urbanski, S., Atlas, E., Campos, T., Shinozuka, Y., Kapustin, V., Clarke, A. D., Weinheimer, A., Knapp, D. J., Montzka, D. D., Holloway, J., Weibring, P., Flocke, F., Zheng, W., Toohey, D., Wennberg, P. O., Wiedinmyer, C., Mauldin, L., Fried, A., Richter, D., Walega, J., Jimenez, J. L., Adachi, K., Buseck, P. R., Hall, S. R., and Shetter, R.: Emissions from biomass burning in the Yucatan, Atmos Chem Phys, 9, 5785–5812, https://doi.org/10.5194/ACP-9-5785-2009, 2009.

Yu, S.: Role of organic acids (formic, acetic, pyruvic and oxalic) in the formation of cloud condensation nuclei (CCN): a review, Atmos Res, 53, 185–217, https://doi.org/10.1016/S0169-8095(00)00037-5, 2000.

Yuan, B., Veres, P. R., Warneke, C., Roberts, J. M., Gilman, J. B., Koss, A., Edwards, P. M., Graus, M., Kuster, W. C., Li, S. M., Wild, R. J., Brown, S. S., Dubé, W. P., Lerner, B. M., Williams, E. J., Johnson, J. E., Quinn, P. K., Bates, T. S., Lefer, B., Hayes, P. L., Jimenez, J. L., Weber, R. J., Zamora, R., Ervens, B., Millet, D. B., Rappenglück, B., and De Gouw, J. A.: Investigation of secondary formation of formic acid: Urban environment vs. oil and gas producing region, Atmos Chem Phys, 15, 1975–1993, https://doi.org/10.5194/acp-15-1975-2015, 2015.

Zellner, R., Exner, M., and Herrmann, H.: Absolute OH quantum yields in the laser photolysis of nitrate, nitrite and dissolved H2O2 at 308 and 351 nm in the temperature range 278-353 K, J Atmos Chem, 10, 411–425, https://doi.org/10.1007/BF00115783, 1990.

Zervas, E., Montagne, X., and Lahaye, J.: C1−C5 Organic Acid Emissions from an SI Engine: Influence of Fuel and Air/Fuel Equivalence Ratio, Environ Sci Technol, 35, 2746–2751, https://doi.org/10.1021/ES000237V, 2001a.

Zervas, E., Montagne, X., and Lahaye, J.: Emission of specific pollutants from a compression ignition engine. Influence of fuel hydrotreatment and fuel/air equivalence ratio, Atmos Environ, 35, 1301–1306, https://doi.org/10.1016/S1352-2310(00)00390-3, 2001b.

Zhang, R., Suh, I., Zhao, J., Zhang, D., Fortner, E. C., Tie, X., Molina, L. T., and Molina, M.

777    J.: Atmospheric New Particle Formation Enhanced by Organic Acids, Sciences, 304, 1487–
778    1490, https://doi.org/10.1126/science.1095139, 2004.

779    Zhang, R., Gen, M., Fu, T. M., and Chan, C. K.: Production of Formate via Oxidation of
780    Glyoxal Promoted by Particulate Nitrate Photolysis, Environ Sci Technol, 55, 5711–5720,
781    https://doi.org/10.1021/acs.est.0c08199, 2021.

782    Zhu, C., Xiang, B., Zhu, L., and Cole, R.: Determination of absorption cross sections of
783    surface-adsorbed HNO3 in the 290-330 nm region by Brewster angle cavity ring-down
784    spectroscopy, Chem Phys Lett, 458, 373–377, https://doi.org/10.1016/j.cplett.2008.04.125,
785    2008.
786

787
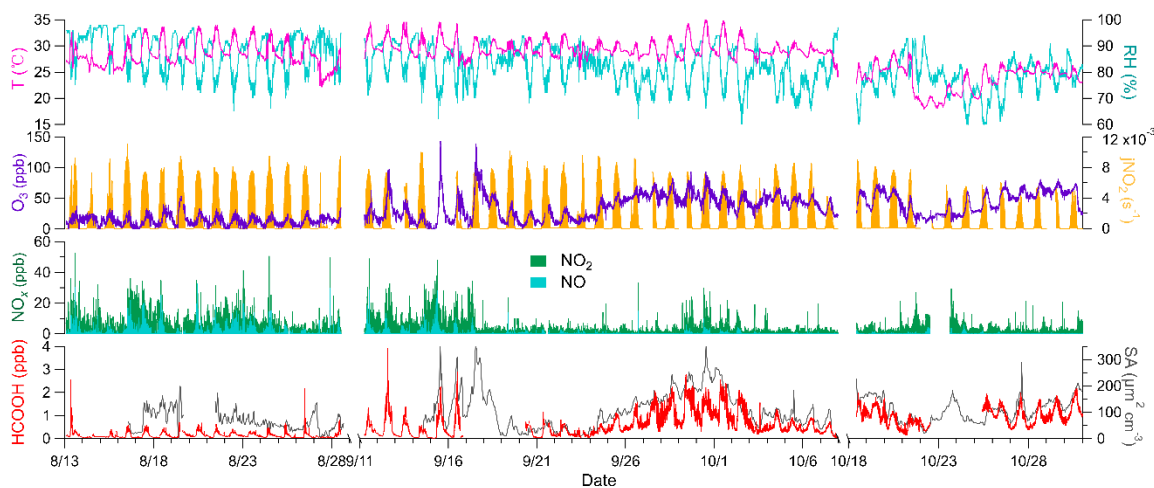
**Fig. 1** Times series of temperature (T); relative humidity (RH); nitrogen dioxide photolysis frequency (jNO₂); concentrations of ozone (O₃), nitrogen oxides (NOₓ), and formic acid (HCOOH); and surface area density (SA) during the field campaign. Data were not collected from August 29 to September 10 due to the persistently clean weather conditions, similar to those during the initial stage of the campaign. The gap in data collection from October 8 to October 17 was due to a rainstorm. Any other short gaps were caused by instrument maintenance.

**Table 1** Summary of worldwide field-observed formic acid (HCOOH) concentrations

| Location | Type | Time | HCOOH (ppb) | Reference |
|---|---|---|---|---|
| Pasadena, USA | urban | 2010.06-07 | 2.0 ± 1.0 | (Yuan et al., 2015) |
| Kensington, London | urban background | 2012.01-02 2012.07-08 | 0.63 (winter) 1.33 (summer) | (Bannan et al., 2017) |
| Shanghai, China | suburban | 2017.06.18-12.23 | 2.08 ± 1.89 | (Xu et al., 2020) |
| Yorkville, USA | rural | 2016.08.15-10.13 | 1.17 ± 0.85 | (Nah et al., 2018) |
| North Pacific | marine | 2008.07.29-08.19 | 30 ± 39.8 ppt | (Miyazaki et al., 2014) |
| Pacific and Atlantic | marine | 2017.09-10 2018.04-05 | < 0.1 | (Chen et al., 2021) |
| Colorado, USA | forest | 2016.02.01-03.01 2016.04.15-05.15 2016.07.15-08.15 2016.10.01-11.01 | 55 ± 57 ppt (winter) 30 ± 24 ppt (spring) 1.2 ± 0.91 (summer) 0.81 ± 0.48 (autumn) | (Fulgham et al., 2019) |
| Alabama, USA | deciduous forest | 2013.06-07 | 2.5 (peak average daytime) | (Millet et al., 2015) |
| Hong Kong, China | coastal | 2021.08.13-10.31 | 0.58 ± 0.53 | This study |

796
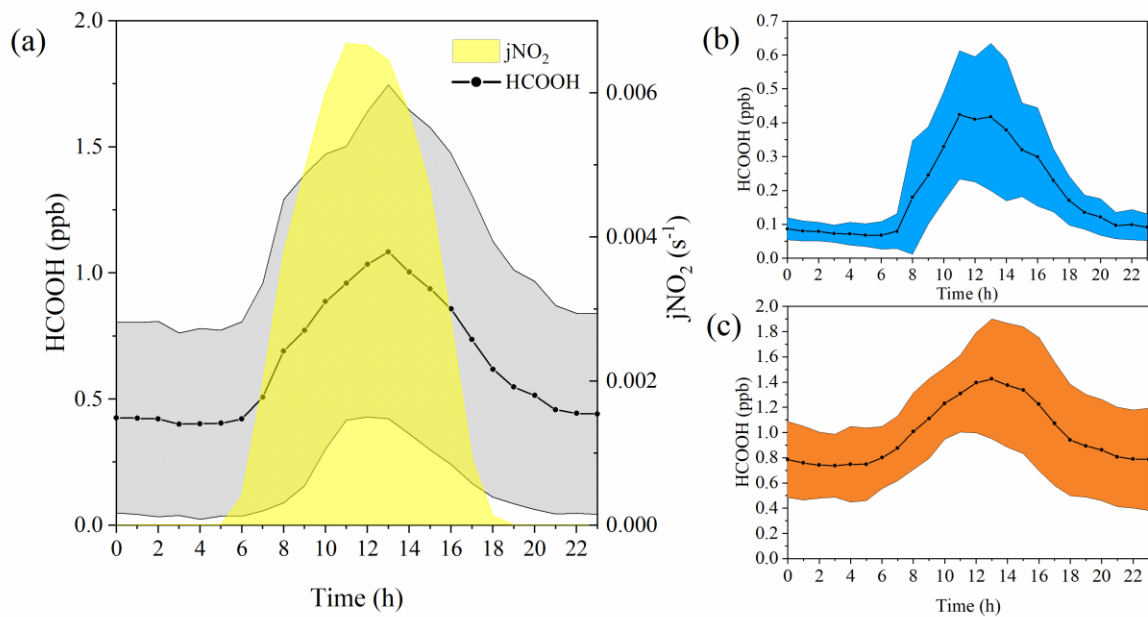
**Fig. 2** Diurnal variation in the concentrations of formic acid (HCOOH) in different periods. (a) Diurnal cycle of HCOOH concentrations and frequency of nitrogen dioxide photolysis ($jNO_2$) for the whole campaign; (b) and (c) diurnal cycle of HCOOH concentrations in marine and coastal air masses, respectively. The shading represents the standard deviations of the measurements.

**Table 2** Pearson correlation coefficient (r) matrix between the concentration of formic acid and other air pollutants, and related meteorological parameters, during three distinct periods.

| Parameter | Coastal | Haze | Marine | Parameter | Coastal | Haze | Marine |
|---|---|---|---|---|---|---|---|
| $jNO_2$ | 0.41 | 0.58 | 0.65 | Sa | 0.73 | 0.68 | -0.03 |
| T | -0.27 | 0.70 | 0.72 | $Sa \times NO_3^-$ | 0.85 | 0.56 | 0.15 |
| RH | -0.56 | -0.51 | -0.65 | $Sa \times O_3$ | 0.83 | 0.74 | 0.31 |
| $PM_1$ | 0.79 | 0.66 | 0.05 | $HNO_3$ | 0.75 | 0.59 | 0.69 |
| $PM_{2.5}$ | 0.69 | 0.63 | 0.19 | $Cl^-$ | -0.41 | -0.44 | 0.09 |
| $PM_{10}$ | 0.68 | 0.55 | 0.26 | $NO_3^-$ | 0.67 | -0.10 | 0.57 |
| HONO | -0.03 | 0.26 | -0.34 | $SO_4^{2-}$ | 0.66 | 0.65 | 0.10 |
| $CH_3COOH$ | 0.89 | 0.88 | -0.27 | $Na^+$ | -0.28 | -0.50 | 0.37 |
| NO | -0.12 | 0.44 | 0.13 | $NH_4^+$ | 0.72 | 0.64 | 0.24 |
| $NO_2$ | -0.24 | 0.36 | -0.39 | $K^+$ | 0.53 | 0.32 | 0.15 |
| $NO_x$ | -0.22 | 0.40 | -0.27 | $Mg^{2+}$ | -0.30 | -0.38 | 0.47 |
| $O_3$ | 0.69 | 0.65 | 0.68 | $Ca^{2+}$ | -0.11 | 0.09 | 0.04 |
| $SO_2$ | 0.64 | 0.66 | 0.41 | HCl | 0.18 | 0.51 | 0.55 |
| CO | 0.63 | 0.51 | 0.13 | isoprene | 0.03 | 0.61 | 0.63 |
| $NH_3$ | 0.37 | 0.46 | 0.16 | benzene | 0.63 | 0.55 | 0.05 |
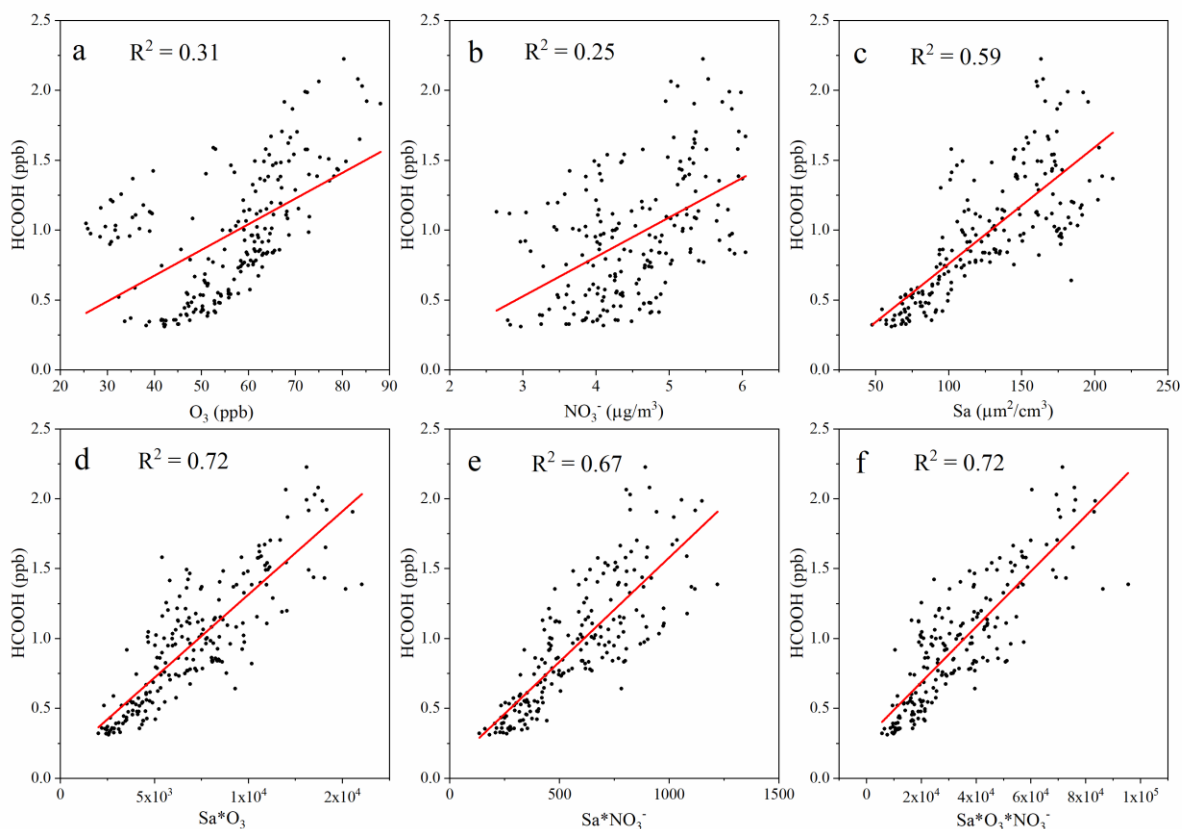
**Fig. 3** Scatter plot of the concentration of formic acid (HCOOH) and (a) the concentration of ozone ($O_3$); (b) the mass concentration of nitrate ions ($NO_3^-$) in $PM_{2.5}$; (c) the surface area density (Sa) of $PM_1$ ($\mu m^2$ $cm^{-3}$); (d) the product of Sa and the concentration of $O_3$; (e) the product of Sa and the concentration of $NO_3^-$; and (f) the product of Sa, the concentration of $O_3$, and the concentration of $NO_3^-$ in coastal air masses.
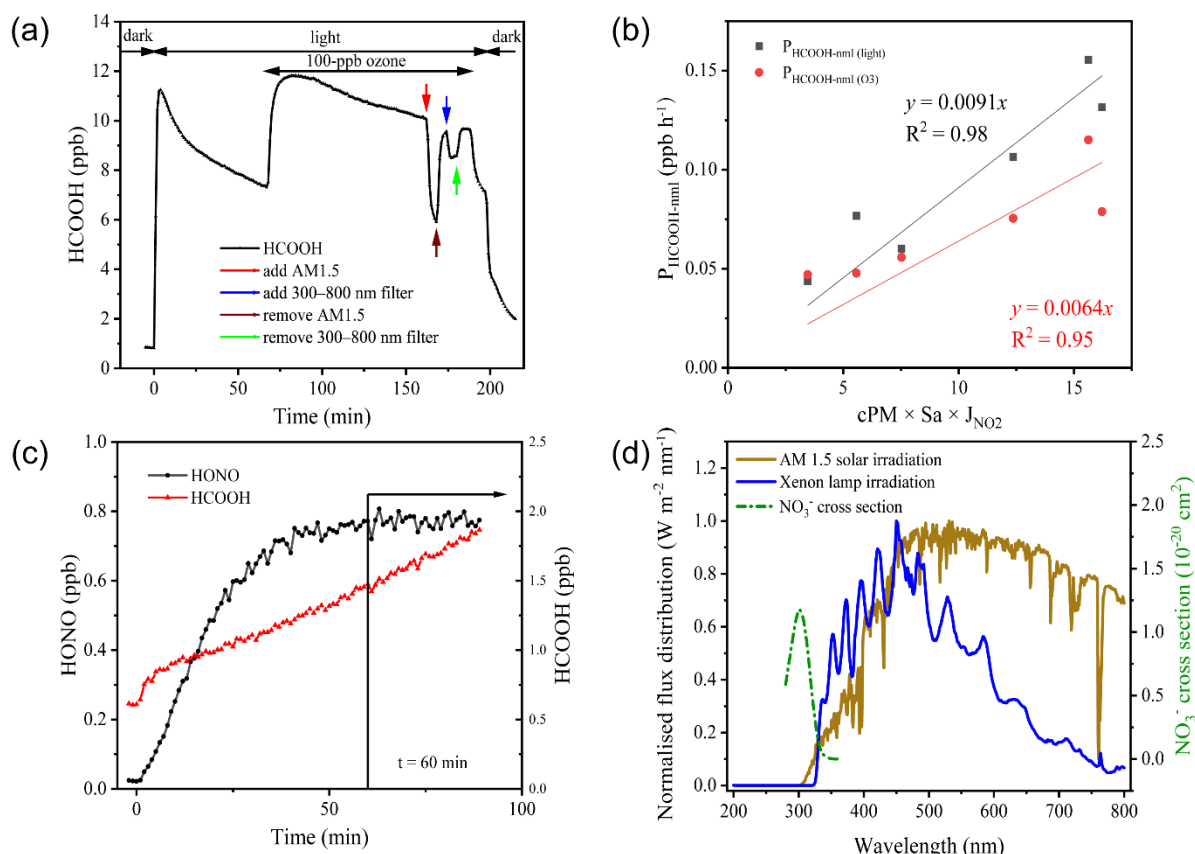
**Fig. 4** Results of the irradiation experiments. (a) Typical variation in formic acid (HCOOH) concentrations during irradiation (in aerosols collected on 2 November 2020). AM 1.5 and 300–800 nm filters were added after the addition of 100-ppb ozone. (b) The correlation between $P_{HCOOH-nml}$ and 2.5-µm particulate matter (PM$_{2.5}$) concentration (cPM) × surface area (Sa) × nitrogen dioxide photolytic frequency (jNO$_2$). (c) Variations in the concentrations of HCOOH and nitrous acid (HONO) as a function of time after illumination of an aqueous solution of formaldehyde and sodium nitrite at pH = 2.7. The vertical black line indicates the time at which HONO stabilised. (d) Comparison of the irradiation spectrum of the xenon lamp used in this study and standard air mass 1.5 solar irradiation (AM 1.5).

**Table 3** Summary of formic acid (HCOOH) concentrations and production rates observed in chamber experiments and normalised HCOOH production rates in ambient air under light and light + ozone (O$_3$) conditions, respectively. HCOOH$_{(O3)}$ denotes the increased concentration of HCOOH after the addition of 100 ppb O$_3$.

| Date | HCOOH$_{(light)}$ (ppt) | HCOOH$_{(O3)}$ (ppt) | $P_{HCOOH(light)}$ (ppt s$^{-1}$) | $P_{HCOOH(O3)}$ (ppt s$^{-1}$) | $P_{HCOOH-nml\ (light)}$ (ppb h$^{-1}$) | $P_{HCOOH-nml\ (O3)}$ (ppb h$^{-1}$) |
|---|---|---|---|---|---|---|
| 2020.10.07 | 8420.2 | 4670.0 | 299.4 | 166.0 | 1.70E-01 | 1.33E-01 |
| 2020.10.08 | 6787.7 | 2899.0 | 241.3 | 103.1 | 1.31E-01 | 7.89E-02 |

| | | | | | |
|---|---|---|---|---|---|
| 2020.10.26 | 4660.9 | 3077.5 | 165.7 | 109.4 | 6.01E-02 | 5.57E-02 |
| 2020.11.02 | 6656.3 | 3507.6 | 236.7 | 124.7 | 1.55E-01 | 1.15E-01 |
| 2020.11.03 | 4490.8 | 2266.7 | 159.7 | 80.6 | 1.06E-01 | 7.55E-02 |
| 2020.11.04 | 4943.1 | 2191.5 | 175.8 | 77.9 | 7.67E-02 | 4.77E-02 |
| 2020.11.05 | 3088.0 | 2368.6 | 109.8 | 84.2 | 4.37E-02 | 4.71E-02 |
| Average | 5578.1 | 2997.3 | 198.3 | 106.6 | 1.06E-01 | 7.89E-02 |

826

827
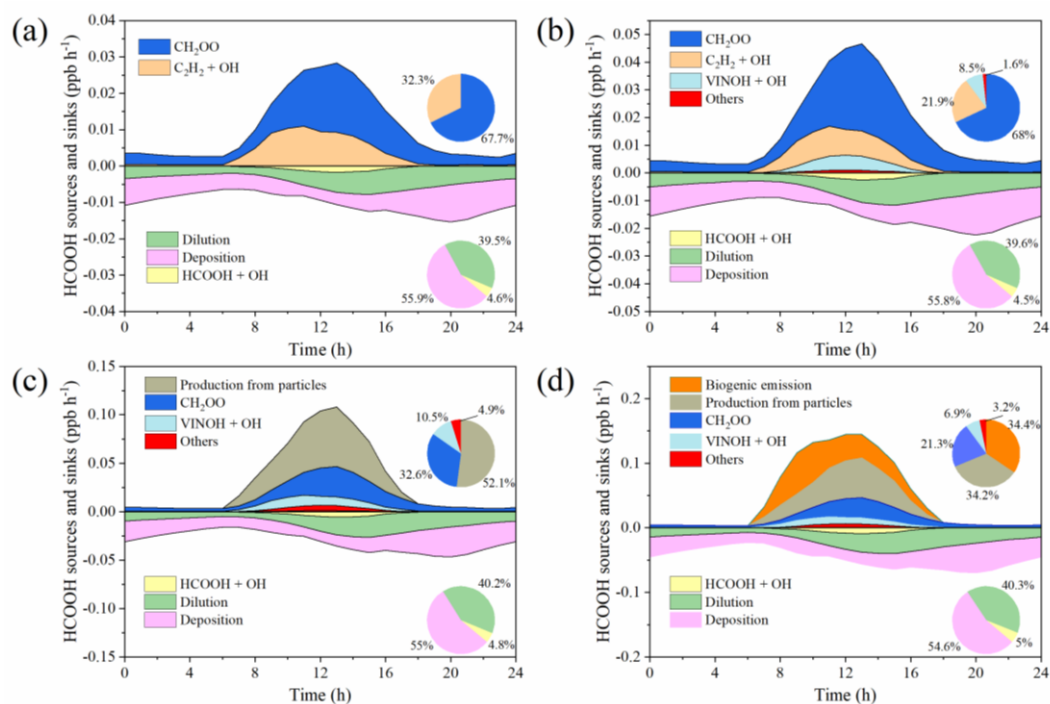
**Fig. 5** Model-calculated profiles of sources and sinks of formic acid (HCOOH) on averaged diurnal profile during the whole campaign in four scenarios described in Table 4. Upper right inset: the contribution from various sources to HCOOH concentrations. Bottom right inset: the contribution from different sinks to HCOOH concentrations. $CH_2OO$ = formaldehyde oxide, a Criegee intermediate (biradical); VINOH = vinyl alcohol.

833
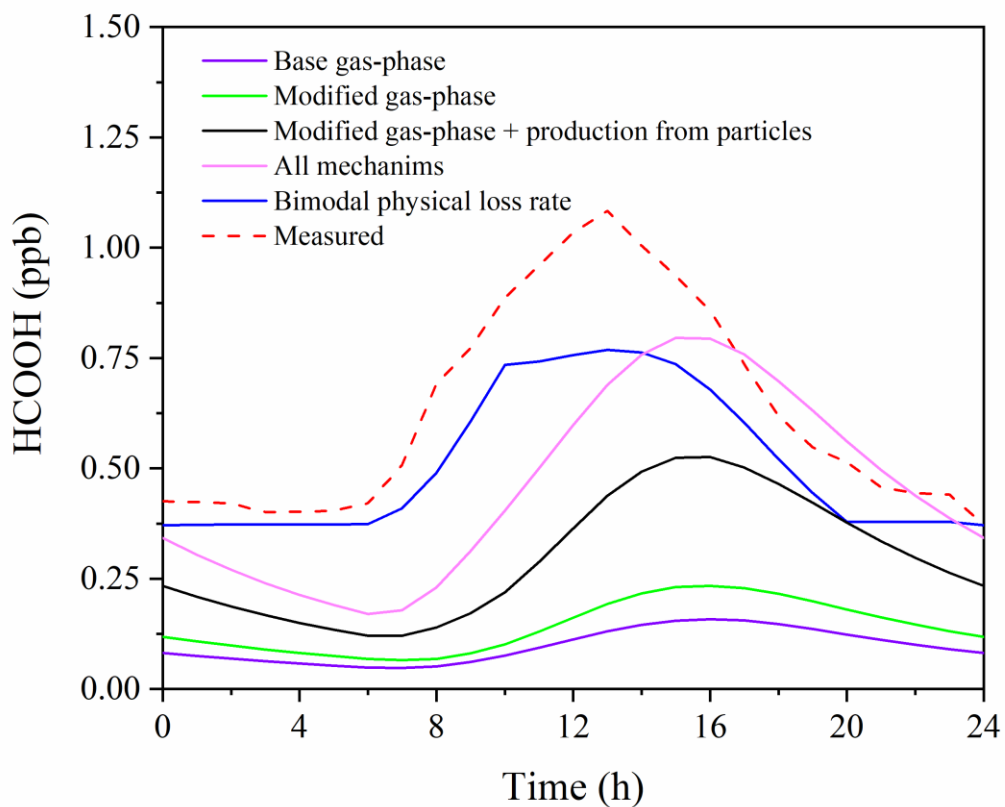
**Fig. 6** Comparison of measured and modelled diurnal profiles of HCOOH during the whole
campaign.

**Table 4** The mechanisms included in different model scenarios.

| scenario | Default MCM | Modified MCM | Particle-phase pathway | Biogenic emissions |
|----------|-------------|--------------|------------------------|--------------------|
| 1 | √ | | | |
| 2 | | √ | | |
| 3 | | √ | √ | |
| 4 | | √ | √ | √ |

837